RSC Advances

ARTICLE

Metal Oxide-Zeolite Composites in Transformation of Methanol to Hydrocarbons: Do Iron Oxide and Nickel Oxide Matter?

Received 00th January 20xx,
Accepted 00th January 20xx

DOI: 10.1039/x0xx00000x

www.rsc.org/

Joshua Mann[a], Valentin Yu. Doluda[b], Clara Leonard[a], Yaroslav B. Losovyj[a], David Gene Morgan[a], Sergey S. Bukalov[c], Zinaida Shifrina[c], Barry D. Stein[d], Nikolay Cherkasov[e], Evgeny V. Rebrov[b,e], Zachary D. Harms[a], Maren Pink[a], , Esther M. Sulman[b], Lyudmila Bronstein[a,c,f]♣

ABSTRACT: The methanol-to-hydrocarbon (MTH) reaction received considerable attention as utilizing renewable sources of both value-added chemicals and fuels becomes number one priority for the society. Here, for the first time we report the development of hierarchical zeolites (ZSM-5) containing both iron oxide and nickel oxide nanoparticles. Modifying the iron oxide (magnetite, Fe_3O_4) amounts, we are able to control the catalyst activity and the product distribution in the MTH process. At the medium Fe_3O_4 loading, the major fraction is composed of the C_9-C_{11} hydrocarbons (gasoline fraction). At the higher Fe_3O_4 loading, the C_1-C_4 hydrocarbons prevail in the reaction mixture, while at the lowest magnetite loading the major component is the C_5-C_8 hydrocarbons. Addition of Ni species to Fe_3O_4-ZSM-5 leads to the formation of mixed Ni oxides (NiO/Ni_2O_3) positioned either on top or next to Fe_3O_4 nanoparticles. This modification allowed us to significantly improve the catalyst stability due to diminishing coke formation and disordering of the coke formed. The incorporation of Ni oxide species also leads to a higher catalyst activity (up to 9.3 g(Methanol)/(g(ZSM-5)×h) and an improved selectivity (11.3% of the C_5-C_8 hydrocarbons and 23.6% of the C_9-C_{11} hydrocarbons), making these zeolites highly promising for industrial applications.

[a] *Indiana University, Department of Chemistry, Bloomington, IN 47405, USA*
[b] *Tver State Technical University, Department of Biotechnology and Chemistry, 22 A. Nikitina St, 170026, Tver, Russia*
[c] *A.N. Nesmeyanov Institute of Organoelement Compounds, Russian Academy of Sciences, 28 Vavilov St., Moscow, 119991 Russia*
[d] *Indiana University, Department of Biology, Bloomington, IN 47405, USA*
[e] *School of Engineering, University of Warwick, Coventry, CV4 7AL, UK*
[f] *King Abdulaziz University, Faculty of Science, Department of Physics, Jeddah, Saudi Arabia*

♣To whom correspondence should be addressed: lybronst@indiana.edu

Electronic Supplementary Information (ESI) available: Nanoparticle sizes, TEM, HRTEM, magnetic measurements data, liquid nitrogen adsorption isotherms, XPS data, and catalytic data. See DOI: 10.1039/x0xx00000x

Introduction

Methanol-to-hydrocarbon (MTH) or methanol-to-gasoline (MTG) reactions received considerable attention as scientists and society are moving towards renewable sources of both chemicals and fuels. Independently of oil prices at the moment, fossil fuels that are currently sources of both valuable chemicals and gasoline, are finite. Typical renewable sources include biomass and biooil. Using pyrolysis and gasification both can be successfully transformed to syngas[1, 2] which, in turn, is used in methanol formation.[3-6]

Zeolite ZSM-5 is a well-known catalyst of MTH and MTG transformations.[7] Although this catalyst was used in the MTG process from early 1970s, its deactivation by coke formation dampened its applications.[7] In recent years several new avenues were developed to prevent coke formation and/or increase the catalyst activity. These avenues include the development of hierarchical zeolites, i.e., zeolites containing both micro- and mesopores,[8-16] minimizing internal framework defects in the zeolite structure,[17] formation of nanosized ZSM particles,[18, 19] etc.

The other approach to improve catalyst stability of ZSM-5 is its modification with various metals. Calcium doping was used for the methanol (or dimethyl ether, DME) to olefin process and at certain Ca loadings it allowed a significant increase of the catalyst stability.[20-22] Modification with Ag, Cu and Ni was found to enhance the selectivity of methanol to C_6–C_{11} aromatic products.[23] It was reported that doping of HZSM-5 with Ni allows for an improvement of catalyst stability against coke formation in the transformation of bioethanol into olefins.[24]

Incorporation of iron oxide nanoparticles (NPs) into zeolites was carried out for magnetic separation or magnetic stabilization,[25, 26] to assist recrystallization of zeolites,[26] and for modification of catalytic properties.[11] To obtain iron oxide containing zeolites several avenues were followed. Iron oxide NPs were (i) added into the solution of a zeolite precursor before a hydrothermal reaction,[25] (ii) formed together with zeolite in the hydrothermal reaction,[11] or (iii) formed in the pores of mesoporous silica followed by dissolution of silica and crystallization of zeolite.[26]

In this work we developed novel, hierarchical zeolites modified with both Fe_3O_4 and Ni_xO_y. Adjusting the iron oxide amounts, we established pathways to control the catalyst activity and the product distribution in the MTH reaction. Doping with Ni_xO_y allowed us to mitigate poor stability of parent zeolites. We demonstrate that the enhanced stability in the MTH process is due to diminishing coke formation and disordering of the coke formed.

Experimental

Materials

Iron (III) nitrate, mesoporous silica gels (6 nm porosity, 200-425 mesh particle size and 15 nm porosity, 200-425 mesh particle size), tetrapropylammonium hydroxide (TPAOH, 1M in H_2O), and Ni (II) acetylacetonate ($Ni(acac)_2$, 95%) were purchased from Sigma-Aldrich and used without purification. Ethylene glycol (99.0%) was purchased from Macron Fine Chemicals and used as received. $NaAlO_2$ was purchased from MP Biomedical LLC and used as received. Ethanol (95%), NaOH, and acetone (99.78%) were purchased from EMD and used without purification.

Synthesis of Fe_3O_4-SiO_2 (FS)

Synthesis of a silica gel filled with iron oxide nanoparticles was performed using a modified procedure described elsewhere.[26] In a typical experiment, 2.5 g of silica gel were added to the solution of $Fe(NO_3)_3$ (see Table 1 for the loadings) in 10 mL of ethanol. The mixture was allowed to stir overnight in air for ethanol evaporation. The sample was then dried in a vacuum oven at room temperature for a minimum of 2 hours until it was entirely dry. The powdered product was then stirred with a spatula while approximately 25 drops of ethylene glycol were added. The sample turned golden-yellow when it has been fully wetted by ethylene glycol. This sample was then loaded into two porcelain boats and heated in a quartz tube in a tube furnace under argon to 250 °C with a heating rate of 2 °C/min. The heating at 250 °C was held for 5 hours and then the sample was cooled to room temperature. The samples synthesized are listed in Table 1. FS stands for Fe_3O_4-SiO_2.

Table 1. Characteristics of Fe_3O_4-SiO_2 and Fe_3O_4-ZSM-5 samples.[a)]

Notations of Fe_3O_4-SiO_2	Iron nitrate loading, g	SiO_2 pore size, nm	Iron oxide NP size, nm	Notation of zeolites	Iron oxide NP size, nm
FS-1	2	6.0	5.5±0.9	FZ-1	5.0±0.8
FS-1	2	6.0	5.5±0.9	FZ-1- calcined	6.2±1.9
FS-2	4	6.0	6.5±1.0	FZ-2	6.6±0.8
FS-3	1	6.0	1.4±0.3	FZ-3	1.6±0.3
FS-4	2	15	6.0±0.6	FZ-4	6.7±1.0
FS-5	4	15	7.4±1.0	FZ-5	8.0±1.3
FS-1	2	6.0	5.5±0.9	FZ-1-Ni[b)]	7.8±2.4
FS-1	2	6.0	5.5±0.9	FZ-1-Ni[b)]-calcined	7.8±2.2
FS-1	2	6.0	5.5±0.9	FZ-1-calcined-Ni[b)]	7.2±2.6

[a)]2.5 g of SiO_2 were used for all syntheses of Fe_3O_4-SiO_2; 0.8 g of Fe_3O_4-SiO_2 were used for all syntheses of Fe_3O_4-ZSM5; for all the samples, 10 mL of ethanol were used; [b)]0.44 g of $Ni(acac)_2$ (per 1 g of FZ-1) were added in 4 mL of acetone.

Synthesis of Fe_3O_4–ZSM5 (FZ)

In a typical procedure, 0.8 g of the Fe_3O_4-SiO_2 composite was transformed to Fe_3O_4-ZSM5.[26] For this, 0.02 g of NaOH and 0.02 g of $NaAlO_2$ were added to the silica precursor. Then, 0.82 g (4.1 mL) of TPAOH was added to the mixture along with 3.8 mL of deionized water. The mixture was stirred in a closed container for 2 hours before being transferred to a Teflon-lined 23 mL Parr Instruments autoclave. The mixture was heated at 180 °C for 24 hours and then allowed to cool to room temperature. The solid product was isolated by centrifugation in test tubes, and washed with deionized water three times and with ethanol once. After ethanol removal, the sample was dried in a vacuum oven overnight. Calcination (when used) has been carried out at 350°C for 4 h in argon followed by 12 h in oxygen. The samples synthesized are listed in Table 1. FZ stands for Fe_3O_4-ZSM5.

Synthesis of Fe_3O_4-ZSM5-Ni

In a typical experiment for incorporation of nickel species with a loading of 10 wt.%, 0.5 g of Fe_3O_4 -ZSM5-N2 (see Table 1) were added to a 50 mL beaker containing 0.2184 g (0.85 mmol) of nickel acetylacetonate and 2 mL of acetone. The suspension was stirred overnight to evaporate acetone and then dried in a vacuum oven for 2 h. After that, the powder was heated in the tubular furnace under argon to 300 °C with a heating rate of 5 °C/min and then held at 300 °C for 2 h. The oven was allowed to cool to room temperature.

Characterization

Electron-transparent specimens for transmission electron microscopy (TEM) were prepared by placing a drop of a sample suspension onto a carbon-coated Cu grid. Images were acquired at an accelerating voltage of 80 kV on a JEOL JEM1010 transmission electron microscope. The images were analyzed with an image-processing package ImageJ (the National Institute of Health) to estimate nanoparticle diameters. High resolution TEM (HRTEM) and scanning TEM (STEM) energy dispersive X-ray spectra (EDS) were acquired at an accelerating voltage of 300 kV on a JEOL 3200FS transmission electron microscope equipped with an Oxford Instruments INCA EDS system. The same TEM grids were used for all analyses.

For scanning electron microscopy (SEM), samples were drop cast onto silicon wafers. They were imaged on a FEI Quanta 600F with the Everhart Thornley detector at an accelerating potential of 2 or 5 kV.

X-ray powder diffraction (XRD) patterns were collected on an Empyrean from PANalytical. X-rays were generated from a copper target with a scattering wavelength of 1.54 Å. The step-size of the experiment was 0.02.

Magnetic measurements were performed on a Quantum Design MPMS XL magnetometer using the systems DC measurement capabilities. Milligram quantities of the sample were placed in a standard gelatin capsule. For zero-field cooling (ZFC) curves, the sample was cooled in a null field (below 0.4 Oe) to 4.5 K. A 50 Oe field was then applied, and measurements were taken at regular temperature increments up to 300 K. The sample was then cooled in the 50 Oe field, and the measurements were repeated at the same temperature increments for the field cooling (FC) curves. These ZFC/FC curves were used to establish the blocking temperature.

X-ray photoelectron spectroscopy (XPS) experiments were performed using PHI *Versa Probe II* instrument equipped with a monochromatic Al K(alpha) source. The X-ray power of 50 W at 15 kV was used for a 200 micron beam size. The instrument work function was calibrated to give a binding energy (BE) of 84.0 eV for the Au $4f_{7/2}$ line for metallic gold, and the spectrometer dispersion was adjusted to give BEs of 284.8 eV, 932.7 eV and of 368.3 eV for the C 1s line of adventitious (aliphatic) carbon present on the non-sputtered samples, Cu $2p_{3/2}$ and Ag $3d_{5/2}$ photoemission lines, respectively. The PHI dual charge compensation system was used on all samples. The ultimate *Versa Probe II* instrumental resolution of 0.125 eV at room temperature was limited by the Fermi edge temperature spread of metallic silver. XPS spectra with an energy step of 0.1 eV

were recorded using software *SmartSoft–XPS* v2.0 and processed using PHI *MultiPack* v9.0 and/or CasaXPS v.2.3.14 at the pass energies of 46.95 eV, 23.5 eV, and 11.75 eV for Fe 2p, C 1s, and O 1s regions, respectively. Peaks were fitted using GL line shapes and/or an asymmetric line shape A(0.2,0.8,0) GL(10), i.e., a combination of Gaussians and Lorentzians with 10-50% of Lorentzian content. A Shirley background was used for curve-fitting. The samples were prepared by drop casting of the NPs solution in chloroform on a native surface of a Si wafer.

Nitrogen adsorption measurements were carried out at liquid nitrogen temperature on an ASAP 2020 analyzer from Micromeritics. Samples were degassed at 100 °C in vacuum. The "t-plot'' method was used to determine the surface area from micropores and estimate the microporous volume.[27] The total surface area was estimated by the Brunauer-Emmet-Teller (BET) method, while the pore size distribution was determined by the *Barrett-Joyner-Halenda* (*BJH*) method using desorption.

For Temperature programmed oxidation (TPO) study, a powdered sample, 16-18 mg, was placed into an U-shaped quartz tube between two layers of quartz wool. The tube was placed into a furnace. Gas flow rates were controlled by Bronkhorst mass-flow controllers. TPO was performed in the flow rate (at standard temperature pressure, STP) of 10 mL/min of 20% O_2 in N_2 containing 1% Ar used as an internal standard. Outlet from the reactor was connected to a Pfeiffer Omnistar quadrupole mass spectrometer. The samples were heated to 650 °C at a heating rate of 5 °C/min.

Raman spectra in the region 100-4000 cm^{-1} were registered using a laser Raman spectrometer LabRAM Jobin-Yvon equipped with a CCD detector and a microscope. Excitation line was 632.8 nm of a He/Ne laser, its output power not exceeding 2 mW.

Catalytic tests

The MTH process was carried out in a continuous mode using a premixer, and two catalytic reactors with a condenser placed between them. In the first reactor, methanol was converted to an equilibrium methanol/DME/water mixture. The condenser was maintained at 4 °C. The condenser allowed for removal of the majority of unreacted methanol and water vapors from the reaction mixture. The gas mixture after the condenser typically consists of N_2, (63.1 vol. %), DME (29.3 vol. %), methanol (1.3 vol.%), water vapors (5.3 vol.%) and small amounts of hydrogen/CO/CO_2 (1.0 vol.%). This mixture is further denoted as DME mixture. The DME mixture was fed to the second reactor where hydrocarbons were formed. The reaction mixture after the second reactor consists of unreacted DME, water, and hydrocarbons including aromatic compounds, olefins, and alkanes.[28, 29]

In a typical experiment, a premixer was filled with 7.3 g of glass beads to mix the nitrogen and methanol flows. The first reactor was filled with 7.3 g of a γ-Al_2O_3 catalyst (0.125-0.134 mm fraction). The second reactor was filled with 100 mg of the zeolite catalyst synthesized. The reactor was placed on a shaker and the catalyst was fed slowly to provide a uniform catalyst distribution throughout the reactor. Prior to the experiment the system was purged with nitrogen (10 mL/min) for 30 min, and then both reactors were heated to the required temperature. After stabilization of the reactor temperature the system was purged with a mixture of 2 vol. % oxygen in nitrogen for 3 h and then with nitrogen for another 30 min. Then liquid methanol was fed at a flow rate of 0.1 mL/min with a HPLC pump. A 1:5 flow splitter was used to obtain the lowest required methanol flow rate of 0.02 mL/min corresponding to a weight hourly space *velocity* (WHSV) of 9.9 g (methanol)/(g(ZSM-5)*h. The reaction gas and liquid mixture was analyzed using an online gas chromatograph (GC) (see the Electronic Supplementary Information, ESI, for details).

During the reaction the nitrogen flow rate was maintained at 10 mL/min (STP). The temperature in both reactors was maintained at 350 °C and the overall pressure was 5 bar. The reaction was carried out for 6 hours. Then the methanol flow was stopped, the reactors were cooled to ambient temperature and the system was purged with nitrogen for 1 h at a flow rate of 10 mL/min. Then the reactors were heated to 350 °C in a mixture of 2 vol. % oxygen in nitrogen and maintained at this temperature for 6 h to complete the catalyst regeneration. Then, the reactors were purged with nitrogen for 30 min and the reaction/regeneration cycles were repeated.

The conversion (C) of the DME mixture to different groups of hydrocarbons was determined as $C=m_{hf}/(m_{DME}+m_{methanol}+m_{ah})*100\%$, where m_{hf} is the mass of a certain hydrocarbon fraction (C_1-C_4, C_5-C_8, C_9-C_{11} (or their sum) or aromatic hydrocarbons), m_{DME} is the mass of DME, $m_{methanol}$ is the mass of methanol, and m_{ah} is the mass of all hydrocarbon fractions. The conversion to a certain hydrocarbon fraction is equal to the selectivity of this fraction.

Results and Discussion

To decouple the influence of iron and nickel oxides on the ZSM-5 structure and catalytic properties in the MTH process, the structure-property relationship was first obtained for the Fe_3O_4-ZSM-5 catalysts and then it was compared with that of the ZSM-5 samples containing both oxides.

Structure of Fe_3O_4-containing ZSM-5

For syntheses of magnetite-containing zeolites, we adapted a procedure, suggested in ref.[26] and consisting of the formation of iron oxide NPs in the silica pores followed by a transformation to iron oxide-zeolite in a hydrothermal reaction. We modified the published method applying it to silica with smaller pores to better control the iron oxide NP

formation as well as varying the amount of the iron precursor. The synthesis conditions of these materials are summarized in Table 1. Figure 1 shows representative TEM images of SiO_2 filled with iron oxide NPs (FS-1, Table 1) and the zeolite obtained in the hydrothermal reaction (FZ-1, Table 1). See the discussion on NP sizes in ESI.

The XRD pattern of silica containing iron oxide NPs shows a broad reflection around 22 two theta degrees which is due to amorphous silica. The positions and intensity of the other Bragg reflections in the XRD pattern of this sample (Fig. 1c) are typical for those of magnetite.[30] However, considering similarity of the XRD patterns of magnetite (Fe_3O_4) and maghemite (γ-Fe_2O_3) NPs due to line broadening, this is a tentative assignment and based on the presence of ethylene glycol (a reducing agent) and argon atmosphere during iron oxide NP formation. The XRD pattern shown in Figure 1d is typical for highly crystalline ZSM-5.[18, 31, 32] For a comparison, see the XRD pattern of 6-ZSM-5 (synthesized without iron oxide NPs from the same silica precursor) in Figure S1 (ESI). For magnetite, only the strongest reflections (311), (511), and (440) are visible, while the other reflections are too weak to be detectable.[26] This analysis is complicated by a very signal-rich pattern of ZSM-5, whose reflections overlap with the reflections of metal oxides.[25, 27]

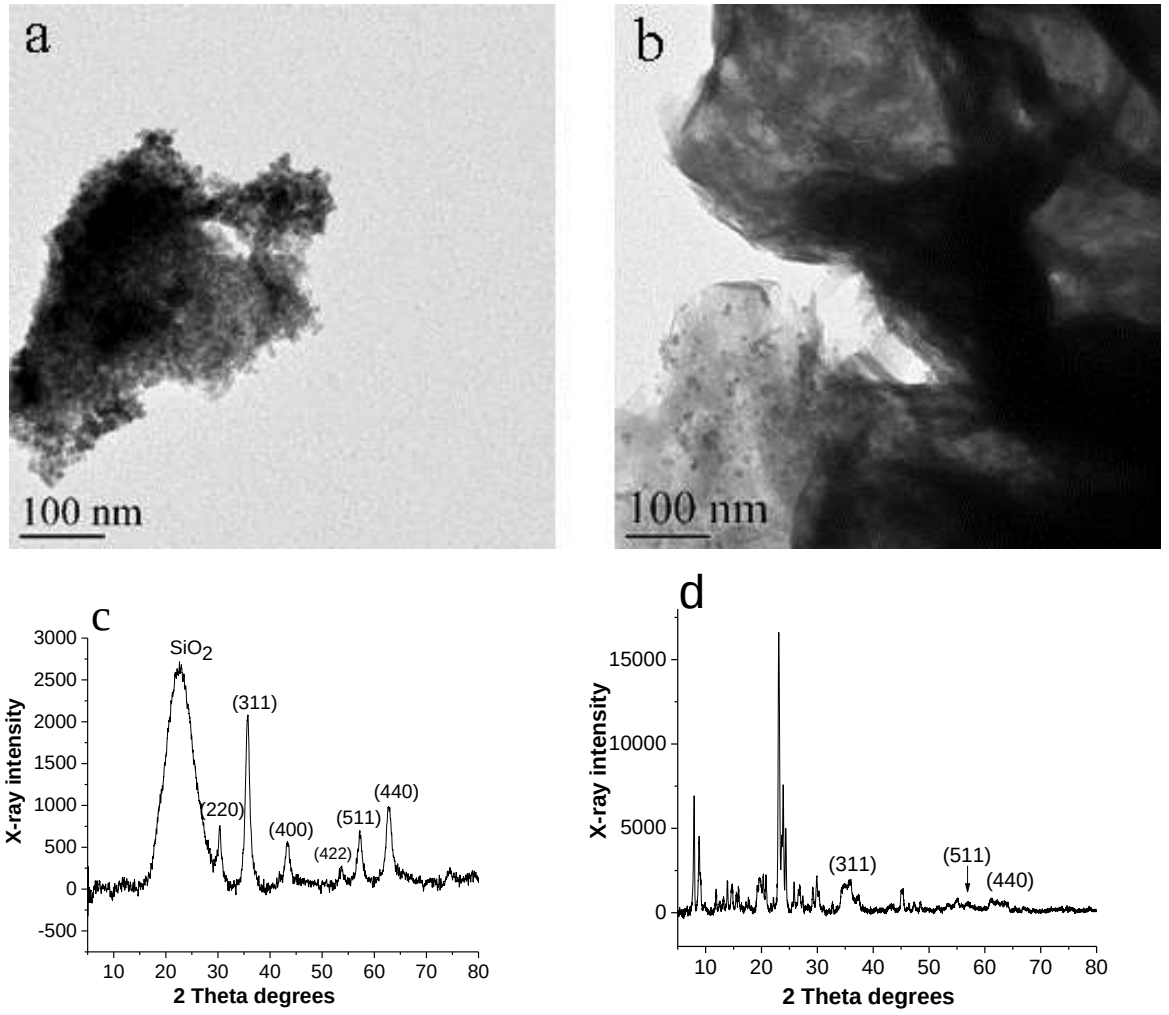

Figure 1. TEM images (a, b) and XRD patterns (c, d) of FS-1 (a, c) and FZ-1 (b, d).

The Fe_3O_4-ZSM-5 catalysts were analyzed by XPS. The survey spectrum of FZ-1 (not shown) reveals the presence of Si, Al, Fe, O, Na, C, and N. Na comes from $NaAlO_2$, while C and N are presumably from a remainder of surfactants in the parent SiO_2. Figure 2 shows a representative high resolution (HR) Fe 2p XPS spectrum of FZ-1. The spectrum displays a main peak with a binding energy (BE) of 711.4 eV which is typical for iron oxides. A weak satellite structure normally observed at a BE value of 8 eV higher than the main peak, is

absent. This satellite indicates the excess of the Fe^{3+} species beyond the Fe^{3+}:Fe^{2+}=2:1 ratio of magnetite.[33-35] In the case of magnetite, the combination of the Fe^{3+} and Fe^{2+} satellites results in a plateau between the Fe 2p3/2 and Fe 2p1/2 peaks,[36] similar to our case.

HR Al 2p and Si 2p XPS spectra of FZ-1 taken at the three randomly chosen spots are shown in Figure 3. According to XPS, the Si/Al atomic ratio is 52 which is known to provide high activity in the MTH reaction.[17]

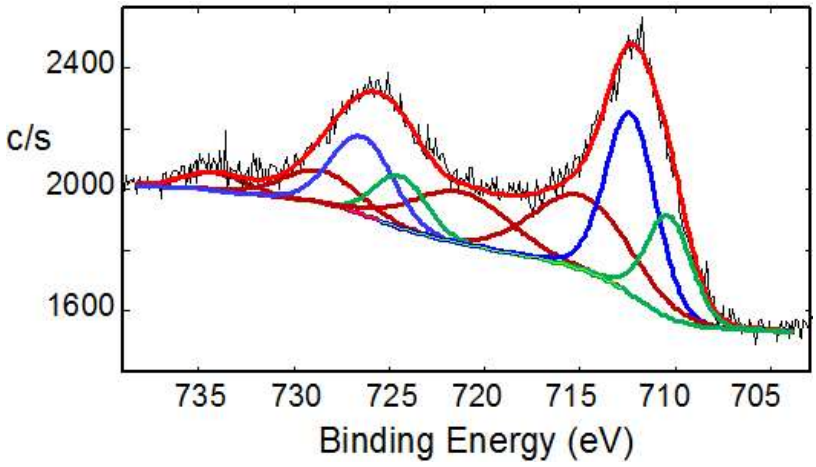

Figure 2. HR Fe 2p XPS spectrum of FZ-1. The data are shown in black; the generated curve is in red; Fe^{2+} and Fe^{3+} are in green and blue, respectively, and brown shows shake-up curves. See Table S1 (ESI) for deconvolution parameters.

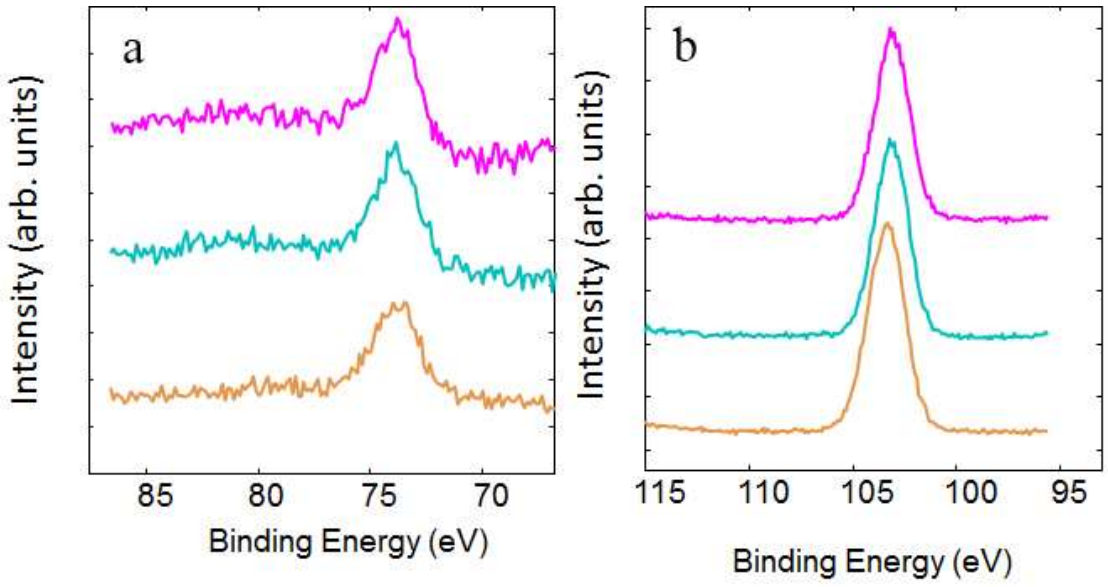

Figure 3. HR XPS spectra of FZ-1 in the Al 2p (a) and Si 2p (b) regions.

Liquid nitrogen adsorption measurements were carried out to assess the porosity of the FZ-1 sample (Table 2 and Figure S1, ESI) and compared with that of 6-ZSM-5.

Table 2. Porosity data for the Fe3O4-ZSM-5 materials.

Sample notation	t-plot micropore surface area, m^2/g	BET surface area, m^2/g	t-plot micropore volume, cm^3/g	BET pore volume, cm^3/g
6-ZSM5	2.2	0.5	0.0010	0.0037
6-ZSM5 calcined	212	204	0.1004	0.0806
FZ-1	8.0	45	0.0031	0.2267
FZ-1 calcined	179	276	0.0826	0.3564
FZ-1-Ni	23	80	0.0097	0.2462
FZ-1-Ni-calcined	107	211	0.0494	0.2500
FZ-1 calcined-Ni	134	216	0.0618	0.2085

Nitrogen adsorption studies demonstrated that the 6-ZSM-5 sample (without iron oxide) has very low microporosity and no mesoporosity. Low microporosity is most likely due to clogging of micropores with the hydrothermal reaction products and remaining surfactants. The absence of mesopores is due to the two factors: (a) no porogen in the transformation of silica to zeolite and (b) dissolution of the parent mesoporous SiO_2 during hydrothermal reaction. The calcined sample exhibits high microporosity but still no mesoporosity. It is worth noting that according to XPS, the parent SiO_2 contains a surfactant residue (data not shown) but apparently its amount is insufficient to allow a mesopore formation. When Fe_3O_4-SiO_2 is used as a precursor in a hydrothermal reaction, the material (FZ-1) also contains low microporosity, but noticeable mesoporosity. As is discussed in ref.[26], the incomplete dissolution of the Fe_3O_4-SiO_2 composite at low alkalinity prevents the escape of Fe_3O_4 NPs from silica gel and allowing for mesoporosity. Figure S1 (ESI) demonstrates that the mean mesopore size in this material is 3.8 nm. After calcination of FZ-1 both micro- and mesoporosity dramatically increase (Table 2) and pore size distribution shows two maxima at 3.8 and 8.0 nm. Larger meso- and macropores are also present in both samples (Fig. S1, ESI), revealing a formation of hierarchical magnetite-zeolites.

The magnetic properties of FZ-1 before and after calcination are discussed in the SI (see Figs. S2 and S3).

Catalytic properties in the MTH process: the Fe_3O_4 influence

Catalytic properties of the materials developed in this work were tested in the MTH process using the two-reactor setup, described in the Experimental section. The separation of the two reactions allows better temperature control due to reduced concentration of methanol in the second reactor and a slower MTH rate as compared to that of methanol dehydration to DME. After the first reactor, the gas mixture mainly contains N_2, DME, methanol, and water (see the Experimental section for the exact composition).

Table 3 presents catalytic activities and selectivities over the fresh 6-ZSM-5 and FZ-1 catalysts and after catalyst regeneration in the fourth consecutive catalytic run. The 6-ZSM-5 catalyst shows moderate activity, but the conversion of the DME mixture to hydrocarbons is rather low (13.2%) with the most abundant gasoline fraction (C_9-C_{11}) of 9.2%. In the four repeat experiments with the same catalyst the methanol conversion rate decreases by 27%, while the conversion to hydrocarbons remains almost unchanged. Surprisingly, the calcined 6-ZSM-5 catalyst shows the same activity trend, but the hydrocarbon yield in the target fraction slightly decreases. Thus, the calcination which frees a large amount of micropores, does not promote the MTH reaction in these catalysts. The importance of zeolite micropores for catalysis is well-known.[37, 38] Apparently, even the non-calcined catalysts have a sufficient amount of micropore entrances where the MHT reaction occurs over Bronsted acid sites. The calcination creates the micropore system further away from the crystal surface that, however, does not affect catalysis.

The presence of iron oxide NPs in the catalyst (FZ-1) allows for a 15% increase of the methanol reaction rate and for a 2.7-fold increase of the DME conversion to hydrocarbons (to 35.2% from 13.2%). In this case, the gasoline fraction increases to 21.7% and the C_5-C_8 fraction increases to 11.1%. Again, the calcination of FZ-1 hardly changes the catalyst performance, although more C_1-C_4 hydrocarbons are formed (6.1 vs. 3.4%). It is noteworthy that calcination increases the Fe_3O_4 NP size from 5.0 to 6.2 nm, revealing that the Fe_3O_4 NP size is hardly a key factor in determining the catalytic properties of magnetite-zeolites, at least in this size range. A double increase of the iron oxide loading (FZ-2, Table S2, ESI, vs FZ-1, Table 3) leads to a significant increase of the C_1-C_4 fraction at the expense of long chain hydrocarbons. Because the Fe_3O_4 NPs have nearly the same size in these two catalysts, it could be concluded that the precursor loading is a major factor which determines the change in selectivity. When the iron oxide loading is decreased by half (compare FZ-1 in Table 3 and FZ-3 in Table S2, ESI), the C_5-C_8 hydrocarbon fraction becomes dominant. In this case, the catalyst contains much smaller Fe_3O_4 NPs (1.6 nm), making it impossible to decouple the influence of the NP size and the Fe precursor loading. However, considering the trend discussed above, we assume that the Fe_3O_4 loading is of paramount importance.

These data clearly indicate that iron oxide *does* influence the catalytic performance, but the question arises what is the possible mechanism of this influence? A number of mechanisms has been discussed in literature as viable paths for the MTH reaction.[39-41] Iron is known to catalyze the

Fischer-Tropsch synthesis.[42] Supported iron-containing NPs showed high activity towards light olefins.[43, 44] Recently, it was also reported that formaldehyde can be formed as an intermediate in the MTH reaction and it may participate in Formose-type reactions leading to carbon–carbon formation and chain growth.[45] At the same time, iron-containing compounds were shown to catalyze a formaldehyde synthesis from methanol.[46, 47] Thus, the Fe_3O_4-ZSM-5 catalysts most likely allow for a higher formaldehyde yield, therefore promoting the chain growth. However, when the catalyst contains a too high fraction of iron oxide NPs, the lighter hydrocarbon formation prevails (similar to a Fischer-Tropsch synthesis).

Although Fe_3O_4 significantly improves the catalyst performance in the first reaction, the advantages are lost in the four consecutive catalytic reactions (Table 3). The decrease of the zeolite catalytic activity in the MTH reaction occurs due to coke formation in the zeolite micropores. Apparently, the presence of Fe_3O_4 NPs does not prevent coking of the catalyst. Moreover, dramatic changes in the product distribution (a much higher fraction of C_1-C_4 hydrocarbons after four consecutive reaction/regeneration cycles) reveal that the microporous network is filled with coke while there is no coke in the close vicinity of Fe_3O_4 NPs. There are several avenues to minimize coke formation including decreasing the size of zeolite particles,[18, 19] creating hierarchical porosity, [8-13] etc. However, the Fe_3O_4-ZSM-5 catalysts already display hierarchical porosity and comparatively small particle size (see Figure S6, ESI and the discussion below). As Ni doping was reported to improve the zeolite stability towards deactivation by coke,[24] we developed zeolites containing both Fe_3O_4 and Ni_xO_y.

Table 3. Catalytic performance of 6-ZSM-5 and FZ-1 in MTH process.[a)]

Parameter	6-ZSM-5 fresh	6-ZSM-5 in 4th cycle	6-ZSM-5 calcined fresh	6-ZSM-5 calcined in 4th cycle	FZ-1 fresh	FZ-1 in 4th cycle	FZ-1 calcined fresh	FZ-1 calcined in 4th cycle
Methanol conversion rate, g(Methanol)/(g(ZSM-5)*h)	6.3	4.6	6.2	4.8	7.4	4.0	7.1	5.1
DME mixture to hydrocarbons conversion, %	13.2	11.4	11.9	4.7	35.2	20.3	34.1	22.9
including C_1-C_4	1.4	1.1	1.4	0.7	3.4	10.4	6.1	11.4
including C_5-C_8	2.6	2.1	2.2	0.8	11.1	3.4	10.8	9.4
including C_9-C_{11}	9.2	8.2	8.3	3.2	21.7	6.3	17.2	2.1
DME to aromatics conversion, %	24.6	16.8	18.7	12.3	18.3	10.3	22.4	8.2

a) Reaction conditions: weight (Al_2O_3):7.3 g, weigth (ZSM-5):0.1 g, liquid methanol flow rate: 0.02 mL/min, nitrogen flow rate:10 mL/min (STP), temperature: 350 °C, pressure: 5 Bar.

Ni-containing Fe_3O_4-ZSM-5: Syntheses and Structure

To prepare a Ni containing Fe_3O_4-ZSM-5 catalyst, the initial Fe_3O_4-ZSM-5 was impregnated with a $Ni(acac)_2$ solution containing a desired amount of $Ni(acac)_2$. This was followed by decomposition of the latter at 300 °C in argon (Table 1). To assess the effect of calcination step on the structure of the Ni-containing Fe_3O_4-ZSM-5 catalysts, two series of experiments were carried out with the calcination step performed either before or after addition of the Ni precursor. The samples were denoted FZ-1-calcined-Ni and FZ-1-Ni-calcined, respectively. The comparison of the porosity data for FZ-1-Ni (Fig. S5, ESI and Table 2) and FZ-1 (Fig. S1, ESI) indicates that after Ni incorporation, the 3.8 nm mesopores are preserved while larger mesopores with the diameter of 14 nm become more prominent. For the calcined Ni-containing samples (Table 2), both microporosity and mesoporosity are dramatically increased, while the pore size distribution remains unchanged (not shown).

The TEM images of FZ-1-Ni at two different magnifications are presented in Figure S6 (ESI). TEM shows that the sample consists of submicron particles (some of them aggregated) composed of rod-like and plate-like particles. The assessment of SEM images (Fig. S7, ESI) of 6-ZSM-5, FZ-1, and FZ-1-Ni reveals that formation of standard zeolite particles with layered structure, typical for the ZSM-5 formation (Figure S7a, ESI),[48, 49] is disrupted in the presence of Fe_3O_4 in the parent silica, leading to much smaller particles. The further post-synthesis procedure of the Ni oxide formation hardly influences the sample morphology, as well as the calcination step (the data are not shown).

From the TEM image analysis it can be concluded that the mean size of iron oxide NPs in the samples increases by 1.0-3.3 nm upon incorporation of Ni species (Table 1). However, TEM images do not allow us to distinguish between magnetite and Ni oxide due to their similar electron density, thus, the increase of the mean NP size can be either due to

deposition of Ni oxide species on top of Fe_3O_4 NPs or due to the formation of larger Ni oxide NPs leading to a broader NP size distribution.

To evaluate the structure of Ni-containing Fe_3O_4-ZSM-5 samples more accurately, STEM EDS of the FZ-1-Ni-calcined sample has been performed. The STEM EDS maps of Si, Fe, and Ni (Figure 4) indicate that Fe and Ni species are evenly spread over the ZSM-5 framework. Moreover, the superposition of the Fe and Ni maps (Fig. 4d) shows that the majority of the Fe and Ni species are in the same locations, revealing that the nucleation of Ni species occurs on the Fe_3O_4 NPs. At the same time, some Fe and Ni species are located side by side, which however, does not preclude the heterogeneous nucleation as well.

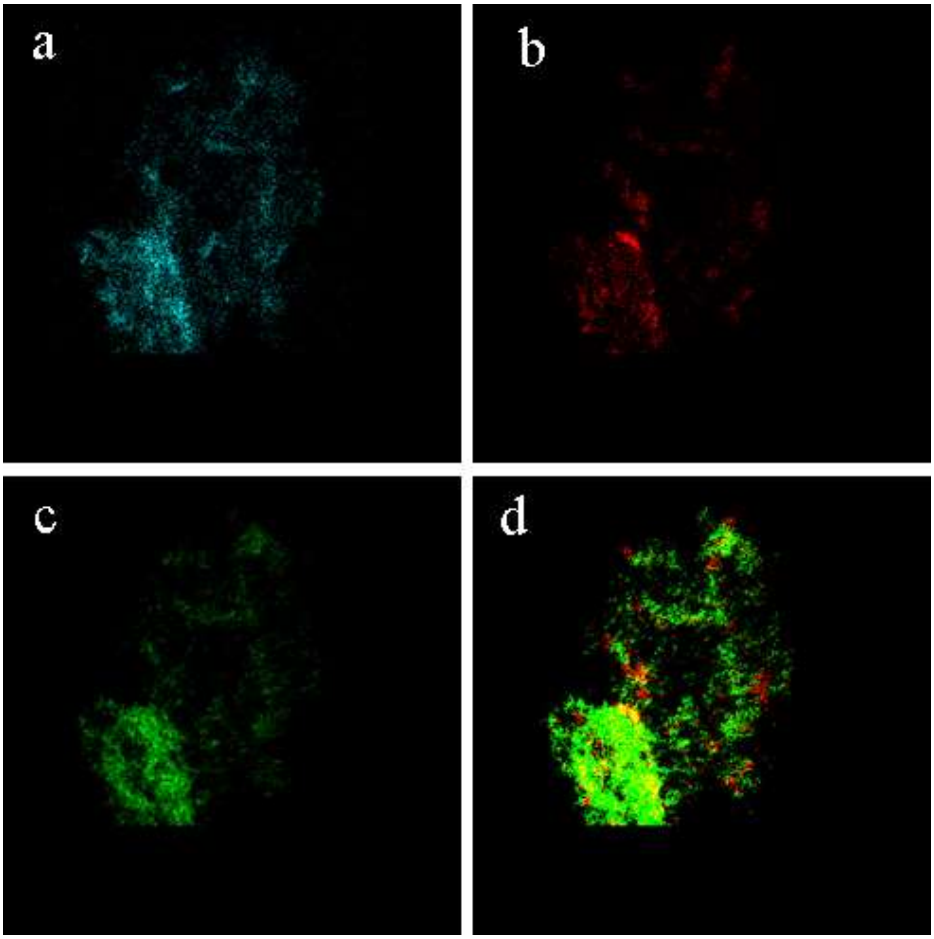

Figure 4. STEM EDS maps of Si (a), Fe (b), Ni (c) in the FZ-1-Ni-calcined sample and the Ni-Fe superposition (d).

The XRD pattern of this sample is presented in Figure S1d (ESI). It shows a typical ZSM-5 pattern similar to that observed for FZ-1 (Fig. S1b, ESI). In the area of weak Fe_3O_4 reflections, a (200) peak is observed which can be assigned to either NiO[50] or Ni_2O_3[51]. Due to low peak resolution in the XRD pattern, it is not possible to distinguish between NiO and Ni_2O_3. Nevertheless, after calcination reflections from both magnetite and Ni oxides become more prominent indicating higher crystallinity compared to the non-calcined sample (see Fig. S1c).

A typical TEM image of the plate-like particle of the FZ-1-Ni-calcined sample is shown in Figure S8 (ESI). It shows a crystalline structure of ZSM-5 with imbedded or attached metal oxide NPs, whose crystallinity is not resolved. The HRTEM image of this sample is presented in Figure 5. It demonstrates that both kinds of nanoparticles (Fe_3O_4 and NiO/Ni_2O_3) are highly crystalline (even despite weak XRD peaks) and in some areas are seen side-by-side, while in other areas both crystalline structures are mixed and cannot be clearly distinguished. This suggests a likely location of Ni oxide on top of the Fe_3O_4 NPs.

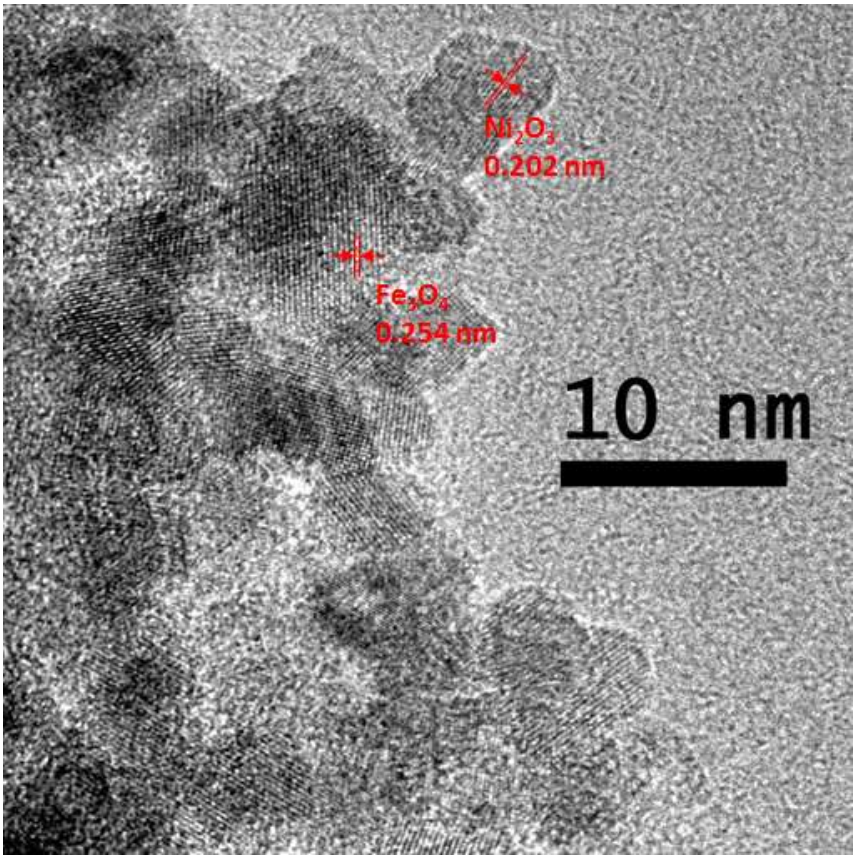

Figure 5. HRTEM image of the FZ-1-Ni-calcined catalyst.

The compositions of three Ni-containing samples obtained from XPS are presented in Table S3 (ESI, see also the associated text). To assess the oxidation state of Ni and Fe and the depth of their penetration, HR XPS spectra were further analyzed. According to deconvolution of the HR XPS Ni 2p spectrum of FZ-1-Ni (Fig. 6), the sample contains both Ni^{2+} and Ni^{3+} with the ratio Ni^{3+}:Ni^{2+}=5.6, confirming the formation of mixed NiO/Ni_2O_3 oxides.

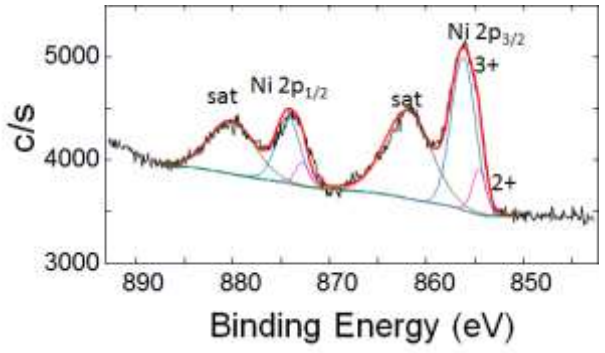

Figure 6. HR XPS Ni 2p of the FZ-1-Ni catalyst. See Table S4 (ESI) for deconvolution parameters.

The HR XPS Fe 2p spectrum of the FZ-1-Ni catalyst is presented in Figure S9 (ESI). Similar to that of FZ-1 (Fig. 2), it shows solely Fe_3O_4 species, indicating that magnetite NPs remain unchanged.

To elucidate the positioning of the Fe and Ni species regarding each other, we compared the XPS data of 2p and 3p electrons for Ni and Fe. It is known that the kinetic energy of 3p photoelectrons is significantly higher than that of 2p electrons, thus, the 3p electrons probe deepest layers versus those producing 2p electrons.[52, 53] We found that the Ni2p/Fe2p ratio is 1.87, revealing that the surface is enriched with Ni species. Alternatively, for 3p transitions, the Ni3p/Fe3p ratio is 0.75, demonstrating that the Ni species are also located at a depth of several nanometers, although their concentration is much lower than that on the zeolite surface. For the Fe species, the trend is reversed. These data indicate that the majority of Ni_xO_y is on top of Fe_3O_4, although some side-by-side location of two types of NPs is also plausible. These data are in a good agreement with HRTEM and STEM EDS.

Catalytic properties: Ni oxide influence

The catalysts modified with 10 wt.% of Ni were studied in the MTH process using the same methodology as that for the Fe_3O_4-ZSM-5 catalysts. Table 4 shows catalytic

performance of three Ni-containing catalysts in the first and fourth consecutive reaction cycles.

Comparison of the catalytic data for FZ-1 (Table 3) and FZ-1-Ni (Table 4) shows that the latter is more active and the catalyst activity remains nearly the same in the fourth reaction/regeneration cycle. Moreover, the conversion to the target hydrocarbon fraction is also higher while there is only a minor change in the product distribution in the fourth reaction/regeneration cycle. When the Ni modifier is added after the sample calcination (FZ-1-calcined-Ni, Table 4), the sample is more active and the catalytic activity does not change with time, but the product distribution does: a high fraction of the C_1-C_4 hydrocarbons is observed in the fourth cycle. Alternatively, the sample calcined after Ni addition (FZ-1-Ni-calcined, Table 4) shows the lowest activity and conversion to hydrocarbons among the three Ni-containing samples, but both activity and the product distribution are exceptionally stable after four catalytic cycles. It is worth noting that the lower Si/Al ratios observed for the three Ni-containing samples compared to that of Fe_3O_4-ZSM-5 (see Table S3 and the text underneath, ESI) have no adverse influence on the catalytic performance.

Table 4. Catalytic performance of the catalysts based on FZ-1 and modified with Ni species in the MTH process. Reaction condition are the same as those in Table 3.

Parameter	FZ-1 fresh	FZ-1 in 4th cycle	FZ-1-Ni fresh	FZ-1-Ni in 4th cycle	FZ-1-Ni-calcined fresh	FZ-1-Ni-calcined in 4th cycle	FZ-1-calcined-Ni fresh	FZ-1-calcined-Ni in 4th cycle
Methanol conversion rate, g(Methanol)/(g(ZSM-5)×h)	7.4	4.0	8.4	8.2	7.6	7.8	9.3	9.4
DME mixture to hydrocarbons conversion, %	35.2	20.3	40.4	47	34.6	35.7	44.1	48.2
including C_1-C_4	3.4	10.4	8.8	14.4	6.2	7.6	9.2	18.7
including C_5-C_8	11.1	3.4	12.4	15.3	11.2	13.4	11.3	13.9
including C_9-C_{11}	21.7	6.3	19.2	17.3	17.2	14.7	23.6	15.6
DME to aromatics conversion, %	18.3	10.3	20.1	19.6	19.4	22.9	23.3	24.0

.

Table S6 (ESI) presents more detailed data for the product distribution in the MTH reaction with 6-ZSM-5, FZ-1, and FZ-1-Ni. These data show that the incorporation of both iron and nickel oxides has only a minor influence on the ratio of the products (both saturated and unsaturated hydrocarbons are observed), although for FZ-1 and FZ-1-Ni, the DME mixture to hydrocarbons conversion is much higher than that for 6-ZSM-5.

The question arises why Ni stabilizes the catalyst performance? The most probable explanation would be that either coke is not formed or it is removed (oxidized) during the catalytic reaction in the presence of Ni oxides. To assess the coke formation, we carried out TPO and Raman spectroscopy measurements for FZ-1 and FZ-1-Ni after the fourth repeated catalytic reaction. In TPO the release of CO_2 and H_2O in a high temperature regime (above 500 °C) is diagnostic of heavy coke consisting of alkylphenanthrenes and alkylpyrenes trapped in the micropores, while the temperature range 200-500 °C is diagnostic of light coke, which is composed of alkylbenzenes strongly adsorbed on Lewis acid sites and silanols on the zeolite surface.[54, 55] The TPO data presented in Table 5 illustrate that for the two catalysts, both light coke and heavy coke are formed, but their amounts are much lower for FZ-1-Ni.

Table 5. TPO data for FZ-1 and FZ-1-Ni after four catalytic reactions.

	CO_2, mmol g-1			H_2O, mmol g-1		
Catalyst notation	<200°C	200-500 °C	>500°C	<200°C	200-500 °C	>500°C
FZ-1	0.12	1.64	0.62	2.96	4.87	0.34
FZ-1-Ni	0.10	2.97	0.06	1.65	4.88	0.12

RSC Advances

ARTICLE

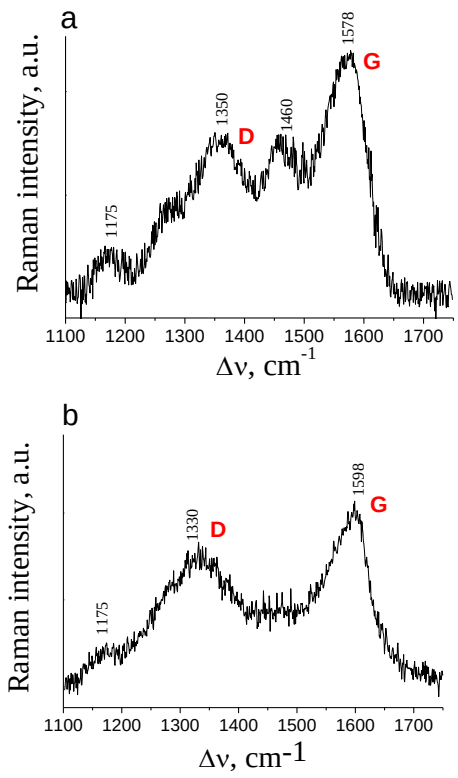

Figure 7. Raman spectra of FZ-1 (a) and FZ-1-Ni (b).

The Raman spectra of the same samples are presented in Figure 7. For both samples, the spectra contain several bands which can be associated with sp^2 carbon. The G band is ascribed to a normal graphite structure, while the D band originates from a defect-containing disordered structure.[56, 57] A more prominent G band vs D band in the FZ-1 spectrum vs those in the spectrum of FZ-1-Ni allows us to assume that the coke in the latter sample has a more disordered character. Presumably, the disordered coke does not obstruct the catalyst surface and easily removed during mild regeneration.

Conclusions

We have demonstrated that the incorporation of the Fe_3O_4 NPs in mesoporous silica followed by a hydrothermal reaction in the presence of an Al source and a structure directing agent (TPAOH) leads to the formation of Fe_3O_4-ZSM-5. Varying the iron precursor loading and the pore size, the magnetite NPs of different sizes were formed. The presence of Fe_3O_4 NPs in ZSM-5 allows one to control the product distribution in the MTH reaction. At the medium magnetite loading, the major fraction is composed of the C_9-C_{11} hydrocarbons (gasoline fraction). At the higher magnetite loading, the C_1-C_4 hydrocarbons prevail in the reaction mixture, while at the lowest magnetite loading the major component is the C_5-C_8 hydrocarbons. The incorporation of Ni species in the Fe_3O_4-ZSM-5 catalysts via impregnation with $Ni(acac)_2$ followed by its thermal decomposition leads to the formation of Ni_2O_3/NiO both on top of magnetite NPs and as side-by-side NPs as is validated by a combination of XPS, HRTEM, and EDS. The presence of Ni species in the Fe_3O_4-ZSM-5 catalysts results in more efficient and more stable catalysts compared to those without Ni due to mitigating the ordered coke formation.

Acknowledgements

The research leading to these results has received funding from the European Community's Seventh Framework Programme [FP7/2007-2013] under grant agreement no. 604296. V.D., E.R. and E.S. thank Russian Science Foundation (project 15-13-20015). Z.S. thanks Russian Foundation for Basic Research (14-03-00876). We also thank the Indiana University Nanoscale Characterization Facility for access to the instrumentation and acknowledge NSF grant #CHE-1048613

Notes and references

1. F. Seyedzadeh Khanshan and R. H. West, *Fuel*, 2016, 163, 25-33.
2. Z. X. Wang, T. Dong, L. X. Yuan, T. Kan, X. F. Zhu, Y. Torimoto, M. Sadakata and Q. X. Li, *Energy & Fuels*, 2007, 21, 2421-2432.
3. S. Polarz, J. Strunk, V. Ischenko, M. W. E. van den Berg, O. Hinrichsen, M. Muhler and M. Driess, *Angew. Chim. Int. Ed.*, 2006, 45, 2965-2969.
4. M. Kurtz, J. Strunk, O. Hinrichsen, M. Muhler, K. Fink, B. Meyer and C. Woell, *Angew. Chim. Int. Ed.*, 2005, 44, 2790-2794.
5. J. Strunk, K. Kaehler, X. Xia and M. Muhler, *Surf. Sci.*, 2009, 603, 1776-1783.
6. N. Baird, Y. Losovyj, E. Y. Yuzik-Klimova, N. V. Kuchkina, Z. B. Shifrina, M. Pink, B. D. Stein, D. G. Morgan, T. Wang, M. Rubin, A. Sidorov, E. M. Sulman and L. M. Bronstein, *ACS Appl. Mater. & Interfaces*, 2016, 8, 891-899.
7. U. Olsbye, S. Svelle, M. Bjorgen, P. Beato, T. V. W. Janssens, F. Joensen, S. Bordiga and K. P. Lillerud, *Angew. Chim. Int. Ed.*, 2012, 51, 5810-5831.

8. Z. Wan, W. Wu, W. Chen, H. Yang and D. Zhang, *Ind. & Eng. Chem. Res.*, 2014, 53, 19471-19478.
9. A. A. Rownaghi and J. Hedlund, *Ind. & Eng. Chem. Res.*, 2011, 50, 11872-11878.
10. Y. Jiao, X. Yang, C. Jiang, C. Tian, Z. Yang and J. Zhang, *J. Catal.*, 2015, 332.
11. F. Zhang, X. Chen, J. Zhuang, Q. Xiao, Y. Zhong and W. Zhu, *Catal. Sci. Technol.*, 2011, 1, 1250-1255.
12. A. A. Rownaghi, F. Rezaei and J. Hedlund, *Micropor. Mesopor. Mat.*, 2012, 151, 26-33.
13. B. Li, Z. Hu, B. Kong, J. Wang, W. Li, Z. Sun, X. Qian, Y. Yang, W. Shen, H. Xu and D. Zhao, *Chem. Sci.*, 2014, 5, 1565-1573.
14. M. Choi, H. S. Cho, R. Srivastava, C. Venkatesan, D.-H. Choi and R. Ryoo, *Nature Mater.*, 2006, 5, 718-723.
15. H. Wang and T. J. Pinnavaia, *Angew. Chem. Int. Ed.*, 2006, 45, 7603-7606.
16. F.-S. Xiao, L. Wang, C. Yin, K. Lin, Y. Di, J. Li, R. Xu, D. S. Su, R. Schlogl, T. Yokoi and T. Tatsumi, *Angew. Chem. Int. Ed.*, 2006, 45, 3090-3093.
17. K. Barbera, F. Bonino, S. Bordiga, T. V. W. Janssens and P. Beato, *J. Catal.*, 2011, 280, 196-205.
18. F. Pan, X. Lu, Q. Zhu, Z. Zhang, Y. Yan, T. Wang and S. Chen, *J. Mater. Chem. A*, 2014, 2, 20667-20675.
19. S. Teketel, L. F. Lundegaard, W. Skistad, S. M. Chavan, U. Olsbye, K. P. Lillerud, P. Beato and S. Svelle, *J. Catal.*, 2015, 327.
20. S. Zhang, B. Zhang, Z. Gao and Y. Han, *Ind. & Eng. Chem. Res.*, 2010, 49, 2103-2106.
21. K. Omata, Y. Yamazaki, Y. Watanabe, K. Kodama and M. Yamada, *Ind. & Eng. Chem. Res.*, 2009, 48, 6256-6261.
22. A. Iida, R. Nakamura, K. Komura and Y. Sugi, *Chem. Lett.*, 2008, 37, 494-495.
23. M. Conte, J. A. Lopez-Sanchez, Q. He, D. J. Morgan, Y. Ryabenkova, J. K. Bartley, A. F. Carley, S. H. Taylor, C. J. Kiely, K. Khalid and G. J. Hutchings, *Catal. Sci. Technol.*, 2012, 2, 105-112.
24. A. G. Gayubo, A. Alonso, B. Valle, A. T. Aguayo, M. Olazar and J. Bilbao, *Chem. Eng. J.*, 2011, 167, 262-277.
25. W. Shan, T. Yu, B. Wang, J. Hu, Y. Zhang, X. Wang and Y. Tang, *Chem. Mater.*, 2006, 18, 3169-3172.
26. B. Li, B. Sun, X. Qian, W. Li, Z. Wu, Z. Sun, M. Qiao, M. Duke and D. Zhao, *J. Am. Chem. Soc.*, 2013, 135, 1181-1184.
27. A. Gervasini, *Appl. Catal. A: Gen.*, 1999, 180, 71-82.
28. Z. Di, C. Yang, X. Jiao, J. Li, J. Wu and D. Zhang, *Fuel*, 2013, 104.
29. A. A. Rownaghi, F. Rezaei and J. Hedlund, *Catal. Comm.*, 2011, 14, 37-41.
30. Y. Tian, B. Yu, X. Li and K. Li, *J. Mater. Chem.*, 2011, 21, 2476-2481.
31. G. Vitale, H. Molero, E. Hernandez, S. Aquino, V. Birss and P. Pereira-Almao, *Appl. Catal. A: Gen.*, 2013, 452.
32. D. Fodor, A. Beloqui Redondo, F. Krumeich and J. A. van Bokhoven, *J. Phys. Chem. C*, 2015, 119, 5447-5453.
33. D. D. Hawn and B. M. DeKoven, *Surf. Interface Anal.*, 1987, 10, 63-74.
34. M. Muhler, R. Schoegl and G. Ertl, *J. Catal.*, 1992, 138, 413-444.
35. T. Yamashita and P. Hayes, *Appl. Surf. Sci.*, 2008, 254, 2441-2449.
36. T. Fujii, F. M. F. de Groot, G. A. Sawatzky, F. C. Voogt, T. Hibma and K. Okada, *Phys. Rev. B.*, 1999, 59, 3195-3202.
37. P. Matias, J. M. Lopes, S. Laforge, P. Magnoux, M. Guisnet and F. R. Ribeiro, *Appl. Catal. A: Gen.*, 2008, 351, 174-183.
38. R. Kumar and B. Chowdhury, *Ind. & Eng. Chem. Res.*, 2014, 53, 16587-16599.
39. U. Olsbye, S. Svelle, M. Bjorgen, P. Beato, T. V. W. Janssens, F. Joensen, S. Bordiga and K. P. Lillerud, *Angew. Chem. Int. Ed.*, 2012, 51, 5810-5831.
40. R. Y. Brogaard, R. Henry, Y. Schuurman, A. J. Medford, P. G. Moses, P. Beato, S. Svelle, J. K. Noerskov and U. Olsbye, *J. Catal.*, 2014, 314, 159-169.
41. M. Zhang, S. Xu, J. Li, Y. Wei, Y. Gong, Y. Chu, A. Zheng, J. Wang, W. Zhang, X. Wu, F. Deng and Z. Liu, *J. Catal.*, 2016, 335, 47-57.
42. S. Soled, E. Iglesia and R. A. Fiato, *Catal. Lett.*, 1990, 7, 271-280.
43. C. Lopez and A. Corma, *ChemCatChem*, 2012, 4, 751-752.
44. H. M. Torres Galvis, J. H. Bitter, C. B. Khare, M. Ruitenbeek, A. I. Dugulan and K. P. de Jong, *Science*, 2012, 335, 835-838.
45. X. Sun, S. Mueller, Y. Liu, H. Shi, G. L. Haller, M. Sanchez-Sanchez, A. C. van Veen and J. A. Lercher, *J. Catal.*, 2014, 317, 185-197.
46. M. Bowker, R. Holroyd, A. Elliott, P. Morrall, A. Alouche, C. Entwistle and A. Toerncrona, *Catal. Lett.*, 2002, 83, 165-176.
47. A. Thivasasith, J. Sirijaraensre, P. Khongpracha, C. Warakulwit, B. Jansang and J. Limtrakul, *ChemPhysChem*, 2015, 16, 986-992.
48. X. Gao, Z. Tang, H. Zhang, D. Ji, G. Lu, Z. Wang and Z. Tan, *J. Molec. Catal. A: Chem.*, 2010, 325, 36-39.
49. Y. Tang, B. Li, N. Zhang, S. Wang, Y. Wen, P. Jin and X. Wang, *CrystEngComm*, 2012, 14, 3854-3857.
50. F. S.-S. Chien, Y. T. Wu, G. L. Lai and Y. H. Lai, *Appl. Phys. Lett.*, 2011, 98, 153513/153511-153513/153513.
51. B. Sasi and K. G. Gopchandran, *Nanotechnology*, 2007, 18, 115613/115611-115613/115619.
52. G. A. Somorjai, in *Chemistry in Two Dimensions: Surfaces*, Cornell University Press, Ithaca, NY, 1981, p. 41.
53. C. J. Powell and A. Jablonski, *J. Phys. Chem. Ref. Data*, 1999, 28, 19.
54. O. Sophiphun, K. Fottinger, S. Loiha, A. Neramittagapong, S. Prayoonpokarach, G. Rupprechter and J. Wittayakun, *Reac. Kinet. Mech. Catal.*, 2015, 116, 549-561.
55. F. Ngoye, L. Lakiss, Z. Qin, S. Laforge, C. Canaff, M. Tarighi, V. Valtchev, K. Thomas, A. Vicente, J. P. Gilson, Y. Pouilloux, C. Fernandez and L. Pinard, *J. Catal.*, 2014, 320.
56. M. Kawakami, T. Karato, T. Takenaka and S. Yokoyama, *ISIJ International* 2005, 45, 1027-1034.
57. B. M. Vogelaar, A. D. van Langeveld, S. Eijsbouts and J. A. Moulijn, *Fuel*, 2007, 86, 1122-1129.

RSC Advances

ARTICLE

TOC graphic and text

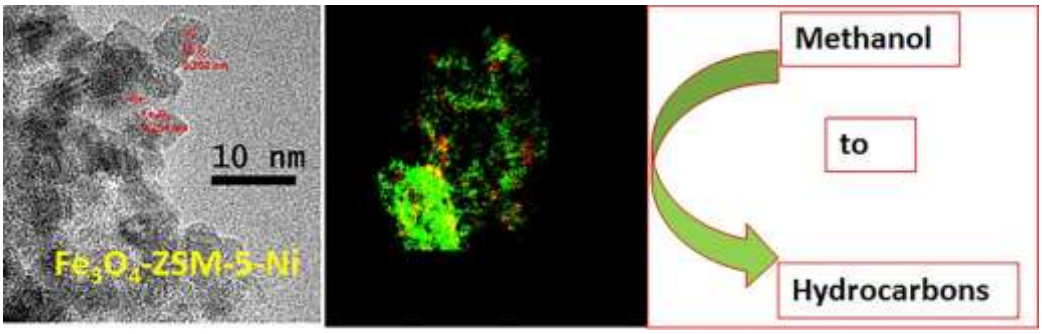

Novel, hierarchical zeolites modified with both Fe_3O_4 and Ni_xO_y nanoparticles have been developed and studied in the methanol-to-hydrocarbon process.